

Research Article

Cite this article: Arjmand S, Catalano R, Oliva D, Amato A, Manna C, Pappalardo AD, Suarez J, Cirrone GAP (2025) Real-time wavelength calibration and multi-technique plasma diagnostics in discharge capillary. *Laser and Particle Beams* **43**, e7, 1–18. <https://doi.org/10.1017/lpb.2025.10004>

Received: 12 May 2025

Revised: 30 July 2025

Accepted: 20 August 2025



Keywords:

emission spectroscopy; gas-filled capillary; imaging spectroscopy; laser-plasma accelerators; Monte Carlo simulation; plasma density; plasma spectroscopy; plasma temperature; wavelength calibration; VHEE therapy

Corresponding author:

Giuseppe Antonio Pablo Cirrone;
Email: pablo.cirrone@lns.infn.it

Real-time wavelength calibration and multi-technique plasma diagnostics in discharge capillary

Sahar Arjmand¹ , Roberto Catalano¹, Demetrio Oliva¹, Antonino Amato¹, Carmelo Manna¹, Alfio Domenico Pappalardo¹, Jose Suarez¹ and Giuseppe Antonio Pablo Cirrone^{1,2,3} 

¹Istituto Nazionale di Fisica Nucleare – Laboratori Nazionali del Sud (INFN-LNS), Catania, Italy; ²Centro Siciliano di Fisica Nucleare e Struttura della Materia (CSFNSM), Catania, Italy and ³Dipartimento di fisica ed astronomia, Università di Catania, Catania, Italy

Abstract

Plasma spectroscopy is a versatile tool for diagnosing key properties of plasmas, including those generated by discharges. It provides critical parameters such as electron density and temperature needed to optimize plasma sources for laser wakefield acceleration (LWFA). Stable, uniform plasma channels are essential to sustain GV/m wakefield and generate high-quality electron beams for advanced applications like radiation therapy (RT). Accurate spectral measurements require reliable wavelength calibration, as optical components can drift with environmental changes. In this study, atomic emission (AE) lamps—specifically mercury (Hg) and neon-argon (Ne-Ar)—were utilized as reference light sources for wavelength calibration of a spectrometer system coupled to an intensified charge-coupled device (ICCD) camera. The known emission lines from these lamps ensured high-precision calibration across the relevant spectral range, facilitating accurate extraction of plasma parameters. This precise calibration enabled the determination of electron density and temperature through spectroscopic diagnostics, which are critical for understanding plasma behaviour. These measurements contribute to the development of gas-filled capillary discharge systems for LWFA and support the experimental objectives of the I-LUCE facility, dedicated to exploring laser-plasma interactions and advancing very high-energy electron beam (VHEE) applications. Monte Carlo (MC) simulations were conducted to assess the dose distribution of VHEE beams for RT applications.

Introduction

Laser wakefield acceleration (LWFA) (Ref. 1) is a specific technique within the broader category of laser-plasma accelerators (LPAs), which themselves are a subset of plasma-based accelerators (PBAs). In LWFA, an intense, ultrashort laser pulse propagates through an underdense plasma, creating a plasma wave- or “wakefield”-behind it. This wakefield possesses electric fields that can be several orders of magnitude stronger than those in conventional accelerators, enabling the acceleration of electrons to high energies over very short distances. Despite these advantages, LPAs face challenges related to beam stability and quality, which currently hinder their ability to fully replace traditional RF systems. A critical factor in overcoming these challenges lies in the plasma source itself: the creation of stable, uniform plasma channels is essential for sustaining high-gradient wakefields and achieving high-quality beam acceleration.

Among the various solutions, gas-filled plasma capillaries provide a flexible approach, allowing fine control over plasma properties. To characterize and optimize these plasma conditions, plasma spectroscopy plays a fundamental role. By analysing spectral line emissions, it is possible to extract key parameters such as electron density and temperature along the capillary axis (Ref. 2). These diagnostics inform the capillary design and ensure plasma uniformity, directly supporting stable and high-quality LWFA experiments. The strategies and diagnostics described above are closely aligned with the objectives of the I-LUCE (INFN-Laser induced UCed Radiation Production) facility (Refs 3, 4, 5), currently under development at the Istituto Nazionale di Fisica Nucleare – Laboratori Nazionali del Sud (INFN-LNS) in Catania, Italy. I-LUCE will provide a dedicated platform for investigating high-power laser-plasma interactions. The facility will feature a high-power laser system capable of accelerating electron beams from the MeV to GeV scale, using either a 460 TW, 23 fs, 2.5 Hz laser or a 45 TW, 23 fs, 10 Hz laser. Gas-filled plasma capillaries will be employed to create tailored plasma channels for LWFA, enabling stable and efficient beam generation to support advances in very high-energy electron beam (VHEE) applications (Refs 5, 6, 7, 8).

© The Author(s), 2025. Published by Cambridge University Press. This is an Open Access article, distributed under the terms of the Creative Commons Attribution licence (<http://creativecommons.org/licenses/by/4.0>), which permits unrestricted re-use, distribution and reproduction, provided the original article is properly cited.

Radiation in discharge plasmas

Radiation in discharge plasmas originates from various dominant emission mechanisms that result from interactions between charged particles (electrons, ions) and neutral atoms. The emitted radiation spans from the ultraviolet (UV) to the infrared (IR) range and includes both continuum and line emission for low-temperature and high-temperature plasmas. The primary mechanisms of radiation in such plasmas include:

- **Line Radiation (Bound-Bound Transitions):**

Occurs when electrons move between specific energy levels in atoms or ions, releasing photons at characteristic wavelengths. In low-temperature, partially ionized plasmas, where atoms or ions are still in the bound state, this is the dominant form of radiation. For example, in hydrogen plasmas, the Balmer series spectral lines, especially H_α and H_β are prominent.

- **Bremsstrahlung Radiation (Free-Free Transitions):**

Occurs when charged particles, mainly free electrons, are decelerated or deflected by the electric fields of other charged particles (ions) in the plasma. This interaction results in the emission of electromagnetic radiation. The intensity of bremsstrahlung radiation depends on both the electron temperature and the plasma density. Although it is most prominent in high-temperature, high-density plasmas—particularly those that are fully ionized with energetic electrons in high-pressure gases (e.g. arcs, fusion).

- **Recombination Radiation (Free-Bound Transitions):**

Occurs when free electrons recombine with ions, forming neutral atoms. The energy released during this process manifests as photons, with energy corresponding to the difference between the electron's kinetic energy and the ion's binding energy. Recombination radiation becomes significant in moderately ionized plasmas, such as in high-pressure arcs or certain laser-produced plasmas, where recombination events are more frequent.

Each of these mechanisms contributes to the overall radiative behaviour of discharge plasmas. Among them, line emission is central to this work, serving as the primary diagnostic tool. By analysing the spectral lines it produces, critical plasma parameters such as electron density, electron temperature, and ionization states can be accurately determined. This is particularly important for plasma diagnostics in LPA applications via LWFA, where precise control of plasma conditions is essential.

Spectroscopic diagnostic

Accurate diagnostics of discharge plasmas are essential for understanding and controlling their properties. Depending on the plasma conditions and expected electron densities, various methods can be applied, such as interferometric methods, mechanical probes (Langmuir), and different spectroscopic methods (absorption, emission, scattering, etc.). This is particularly important in compact configurations, where the plasma may be confined to dimensions of approximately 2 mm to 100 μm , or in optically thin plasmas. In such cases, mechanical probes are impractical, as they can disturb local plasma conditions. Instead, non-intrusive, real-time diagnostic techniques are required to provide reliable information without affecting the plasma.

Among spectroscopic techniques, optical emission spectroscopy (OES) stands out as one of the most effective non-contact

methods for diagnosing discharge plasmas. By analysing the light emitted from excited atoms and ions, OES enables the measurement of key plasma parameters such as electron density, electron temperature, and ionization degree. It also allows identification of the species present in the discharge through their unique spectral signatures. Due to its non-intrusive nature, OES is particularly advantageous in scenarios where maintaining plasma integrity is crucial, such as in compact or optically thin plasmas. OES is typically implemented using either spectrometers or monochromators. Spectrometers provide the full emission spectrum, supporting broad analysis and species identification. Monochromators, equipped with diffraction gratings, isolate individual wavelengths for detailed study of specific spectral lines. In both approaches, accurate calibration is essential to ensure precise and reliable diagnostics.

Time-resolved imaging spectroscopy

Various diagnostic techniques are used in the OES and plasma analysis, each for specific measurement goals. These include time-resolved spectroscopy with intensified charge-coupled device (ICCD) detectors for transient phenomena, fibre-optic and slit-scanning spectroscopy for spatial-spectral mapping, and monochromatic imaging for specific emission lines. Time-resolved imaging spectroscopy is particularly valuable for capturing both spatial and spectral information simultaneously, ideal for studying dynamic behaviours and non-uniformities in plasmas.

For reliable spectral measurements, imaging spectrographs require precise wavelength calibration. This calibration ensures that the recorded spectra are accurately mapped to their corresponding wavelengths, which is essential for identifying emission lines and extracting quantitative plasma parameters such as electron density and temperature.

Calibration methods include using spectral lamps, monochromators, tunable lasers, or gas cells. While monochromators and tunable lasers are more complex and costly, spectral lamps provide a simpler solution, covering a broad range such as the visible spectrum. Wavelength calibration is essential for ensuring the alignment of a spectrometer's spectral response with known reference wavelengths, minimizing errors. Continuous evaluation of calibration performance is crucial for high-precision applications like laser-plasma interaction studies and time-resolved diagnostics, ensuring sustained accuracy over time. Even slight deviations in the relationship between spectral pixel indices and wavelengths can significantly impact spectral interpretation. Although many instruments show an approximate linear relationship, deviations may occur because of instrumental imperfections or optical aberrations.

A key component in spectrometers, the diffraction grating, disperses light by causing constructive interference at specific angles, as described by the grating equation (Ref. 9):

$$m\lambda = d (\sin\alpha + \sin\beta), \quad (1)$$

where m : diffraction order, λ : wavelength of the light, d : spacing between the grating grooves, α : incident angle (the angle at which light strikes the grating), β : diffraction angle (the angle at which light is dispersed and detected).

The relationship between the diffraction angle β and the wavelength λ is generally small and is often approximated as linear. However, this relationship is not strictly linear. By solving

Table 1. Specification of the SpectraPro HRS-300 PI spectrograph

Parameter	Specification
Focal length	300 mm
Aperture ratio	f/3.9
Inclusion angle	30.4°
Detector angle	1.38°
Turret	Triple-grating interchangeable
Slit width	0.01–3 mm
Slit height	4–14 mm
Ruled grating	600 g/mm (500 nm Blaze)
Blazed grating	1200, 2400 g/mm (Holographic VIS Blaze)
Grating size	68 mm × 68 mm
CCD spectral resolution	0.1 nm
Scan range	0–1500 nm
Wavelength range with 1200 g/mm	60 nm
Wavelength range with 2400 g/mm	30 nm

the grating equation for $\beta(\lambda)$, the diffraction angle is given by (Ref. 10):

$$\beta(\lambda) = \arcsin\left(\frac{m\lambda}{d} - \sin\alpha\right). \quad (2)$$

The relationship is approximately linear near zero, though deviations from perfect linearity may arise. These deviations are primarily caused by misalignments in the grating and optical aberrations in the lenses, which can alter the diffraction angles.

Spectroscopic system setup

The spectroscopic system used in this study includes a spectrograph, detector, light source, and auxiliary optics. Princeton Instruments (PI) SpectraPro HRS-300, optimized for the visible wavelength range (approximately 400–700 nm), was used for spectral analysis. Its specifications are detailed in Table 1.

The spectrograph system incorporates interchangeable grating turrets to accommodate various spectral applications. It also features the IntelliCal wavelength calibration light source, a compact, USB-powered unit that combines mercury (Hg) and neon-argon (Ne-Ar) emission lamps within a single housing. These lamps emit stable and well-characterized spectral lines, facilitating precise and repeatable calibration. The IntelliCal unit can be mounted directly to the spectrograph's entrance slit for routine calibration or repositioned for in situ alignment checks, thereby minimizing experimental downtime. A front-panel toggle switch allows for quick lamp selection, and an accompanying emission-line reference chart ensures traceable wavelength validation, essential for resolving sub-nanometre spectral features. The spectrograph separates the incoming light into different wavelengths, which are recorded using an Andor iStar DH320T Gen 3 time-resolved image intensifier connected to an ICCD camera. The ICCD detector features a 1024×255 pixel matrix with an effective pixel size of $26 \times 26 \mu\text{m}$, providing high spatial and spectral resolution.

This configuration enables both time-resolved measurements (with a minimum gate width of 2 ns) and precise spectral sampling, which is critical for capturing transient phenomena such as laser-induced plasmas or fluorescence decay.

The spectrograph incorporates three interchangeable gratings, each optimized for specific resolution and wavelength coverage. While the detector theoretical range spans 0–1500 nm, practical operation is constrained by factors such as grating efficiency, optical component transmission, slit aperture geometry, and the ICCD's quantum efficiency.

High-resolution configurations utilize a 1200 grooves/mm (g/mm) grating, providing a 60 nm spectral window per acquisition, or a 2400 g/mm grating, yielding a 30 nm window. The 1024 horizontal pixels of the ICCD, combined with the $26 \mu\text{m}$ pixel pitch, translate to a spectral sampling density of ~ 0.06 nm/pixel for the 1200 g/mm grating. This ensures fine resolution of narrow spectral features, while the 2400 g/mm grating further enhances resolving power, ideal for applications such as Raman spectroscopy or resolving atomic emission lines. The inverse relationship between groove density and spectral coverage highlights the adaptability, balance resolution, and range of the system for targeted experimental needs.

Data acquisition

To ensure accurate wavelength calibration within the 400–700 nm range, we used emission lines from mercury (Hg: 400–580 nm) and neon-argon (Ne-Ar: 580–700 nm) lamps, chosen for their distinct and stable lines. The IntelliCal light source, integrating both lamps mounted directly to the entrance slit, facilitated the calibration. During the calibration process, the spectrometer was configured with a 1200 g/mm diffraction grating, operating in the first diffraction order ($m = 1$). The light source was positioned in front of the spectrometer's entrance slit, and each lamp – either a Hg or Ne-Ar lamp – was illuminated sequentially to collect spectral images. The exposure time for each lamp was adjusted to ensure an adequate signal without causing overexposure. It varied according to the intensity of the light emitted by each lamp. The Ne-Ar lamp, which typically emits more intense lines, required shorter exposure times to avoid saturation, whereas the Hg lamp, with less intensity, necessitated longer exposure times for optimal image capture. An example of a detected spectral frame is presented in Figure 1.

Identifying spectral lines

The spectrometer was set up with a 1200 g/mm grating to achieve high spectral resolution across the 400–710 nm visible range, using both Hg (blue colour) and Ne-Ar (red colour) lamps. Figure 2 shows the overlaid spectra of this range.

However, to do this, the full range was divided into five separate intervals, each spanning 60 nm, because of the spectrometer's limited spectral window per acquisition. For each interval, the spectrometer was calibrated by setting the central wavelength near the midpoint of the target lines. This approach allowed for the observation of two to six emission lines per interval, depending on the lamp used.

The number and distribution of lines varied by lamp type. The Hg lamp, with relatively few lines, typically exhibited two to three lines per 60 nm window. In contrast, the Ne-Ar lamp produced a denser distribution, especially in the red and near-infrared regions, enabling up to six lines per interval. To optimize spectral coverage, the wavelength intervals were centred on the densest groupings



Figure 1. An example of detected spectral frame showing Ne-Ar emission lines in the 620–660 nm range.

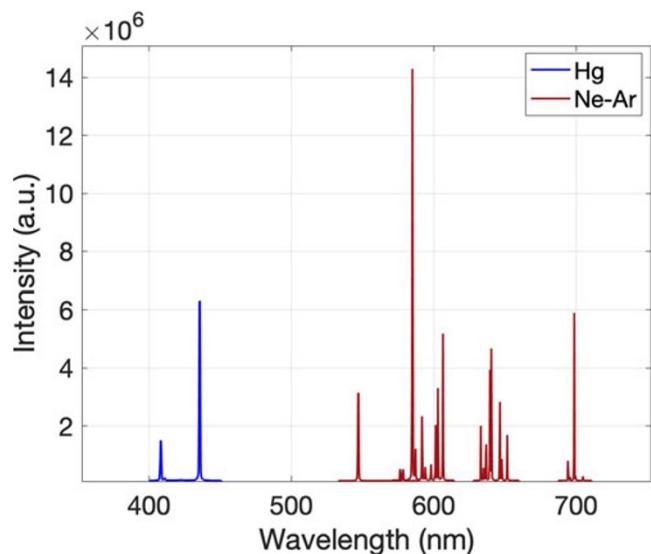


Figure 2. Overlaid spectra from five intervals covering 400–710 nm.

of lines within each lamp emission range. The measured emission lines were identified and verified using reference values from the NIST database (Ref. 11), confirming both line identification and wavelength calibration. Figure 3 displays the recorded spectra from five intervals, highlighting variations in line density between sources: blue for Hg and red for Ne-Ar.

To evaluate the accuracy of the wavelength calibration, two complementary analyses were conducted: a point-by-point deviation assessment and a statistical error quantification. Each measured wavelength was compared with its corresponding reference value, and the deviations are illustrated in Figure 4. As shown, almost 50% of the deviations fall within the range of ± 0.1 – 0.5 nm, indicating a reasonable calibration accuracy which for precise spectroscopy (e.g. Stark broadening, Doppler shift) the acceptable deviation must be $< \pm 0.2$ – 0.5 nm.

To quantitatively assess the overall calibration quality, the mean absolute error (MAE) was computed:

$$\overline{\Delta\lambda} = \frac{1}{N} \sum_{i=1}^N |\Delta\lambda_i|, \quad (3)$$

where N is the total number of emission lines used in the calibration, and $\Delta\lambda_i$ is the difference between the measured and reference wavelengths for the i th emission line. The calibration quality can be assessed on the basis of the MAE:

- MAE ≤ 0.5 nm: high accuracy, sufficient for most spectroscopic applications,
- MAE ≥ 1 nm: potential systematic errors that require correction or higher order fitting.

The measured MAE of ≈ 0.5 nm indicates a high calibration accuracy. The remaining error likely stems from the employing of multiple separate spectral intervals, which can introduce inconsistencies due to varying sampling intervals. However, for studies focused on specific spectral lines, particularly the characterization of hydrogen plasma via the $H\alpha$ or $H\beta$ lines, a more targeted calibration approach is feasible. By focusing on a specific spectral region and employing a single calibration interval, the accuracy can be enhanced, potentially reducing the MAE. In summary, while the current calibration provides good accuracy with minor deviations, adopting a localized calibration strategy for the spectral region of interest could further improve precision.

Pixel-to-wavelength mapping

After identifying emission lines in the captured spectra and recording their corresponding pixel positions on the detector, we established a precise wavelength calibration. Figure 5 presents the five spectral intervals with their corresponding pixel positions.

This pixel-to-wavelength mapping process involved establishing a linear relationship between pixel positions and wavelengths using known reference lines. For each interval, we model the wavelength λ as a function of the position of the pixels p :

$$\lambda = S \cdot p + b, \quad (4)$$

where S is the dispersion coefficient or slope (wavelength change per pixel), and b is the intercept (wavelength at pixel zero). The mapping approach varied by interval based on the number of identifiable emission lines:

- Intervals 2 and 5 contained only one identifiable emission line, making linear regression impossible; these were excluded from calibration,
- Intervals with two reference lines used direct linear interpolation: $S = \frac{\lambda_2 - \lambda_1}{p_2 - p_1}$,
- Intervals with more than two lines employed least-squares regression to account for potential nonlinearities.

Figure 6 demonstrates this piecewise mapping approach, showing linear fits for intervals 1, 3, and 4. The variation in slopes across intervals (ranging from 0.037 to 0.193 nm/pixel) indicates moderate changes in spectral resolution across the detector. While the interval with the smallest dispersion coefficient (0.037 nm/pixel) offers the highest resolution, the overall variation is sufficiently small that it has negligible impact for most practical applications where spectral lines are not extremely closely spaced. However, it is important to note that the same pixel position corresponds to different wavelengths in different intervals. Additionally, the wavelength change per pixel (resolution) varies across the spectral range, meaning that each interval requires its own distinct calibration parameters.

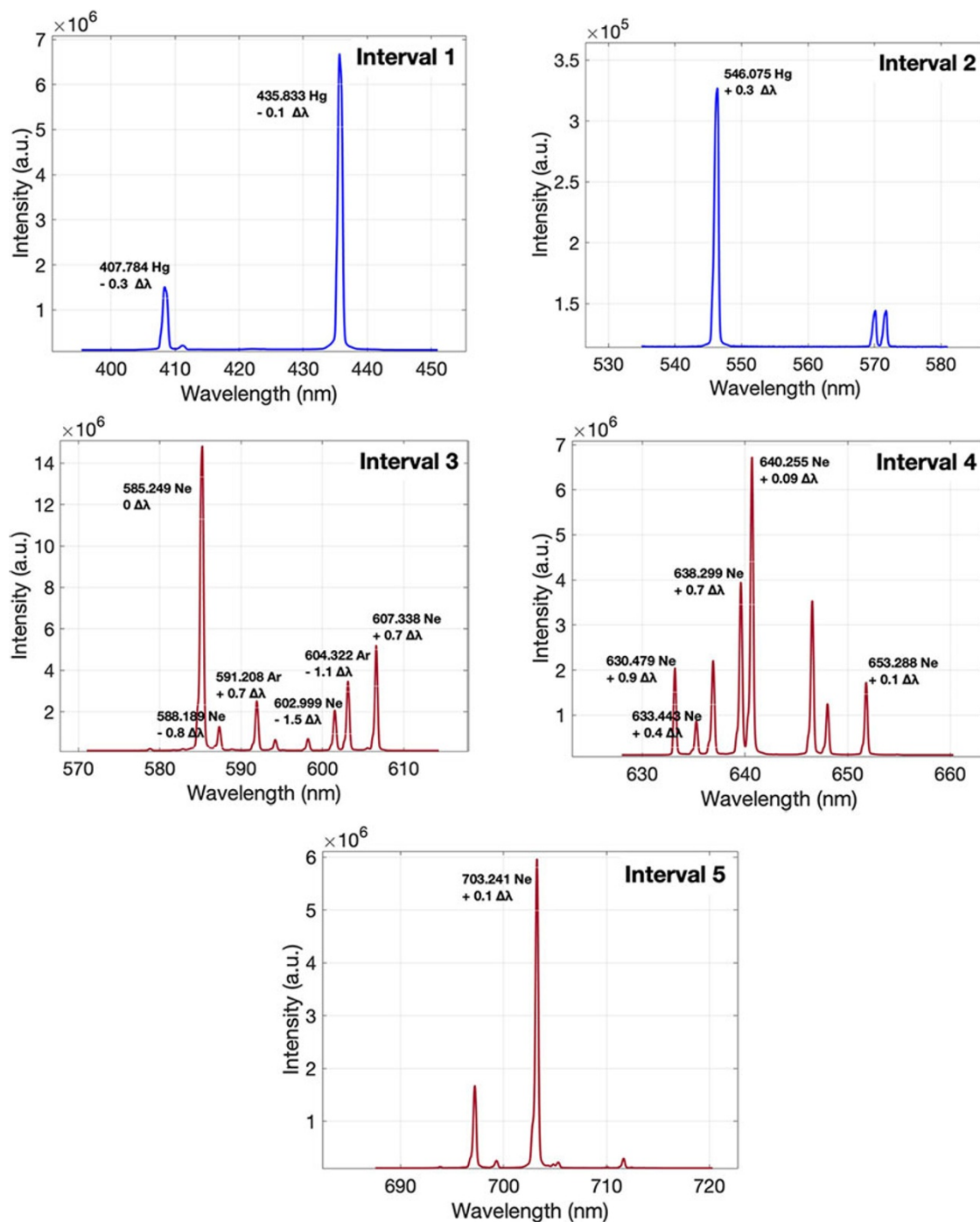


Figure 3. Observed spectrum of calibration lamps, including Hg (blue) and Ar-Ne (red) from 5 intervals, showing the line output.

Table 2 presents the complete calibration results, including pixel positions, reference wavelengths, measured wavelengths, and their deviations for both Hg and Ne-Ar lamps across five spectral intervals.

Plasma imaging: Image formation and calibration

To tease out the generated plasma require capturing both spectral and spatial information, enabling the recovery of the plasma distribution along the capillary channel. This is achieved using a

spectrometer coupled with a fast-gated ICCD camera, which offers a resolution of 1024×255 pixels. The setup enables the simultaneous recording of wavelength-resolved light (horizontal axis) and spatially-resolved emission along the plasma channel (vertical axis), producing a two-dimensional (2D) image of the plasma. The formation of the 2D image recorded by the ICCD captures both spectral and spatial dimensions of the plasma emission. Then, to extract physical information from the ICCD image, calibration procedures are required to convert pixel indices into physical units.

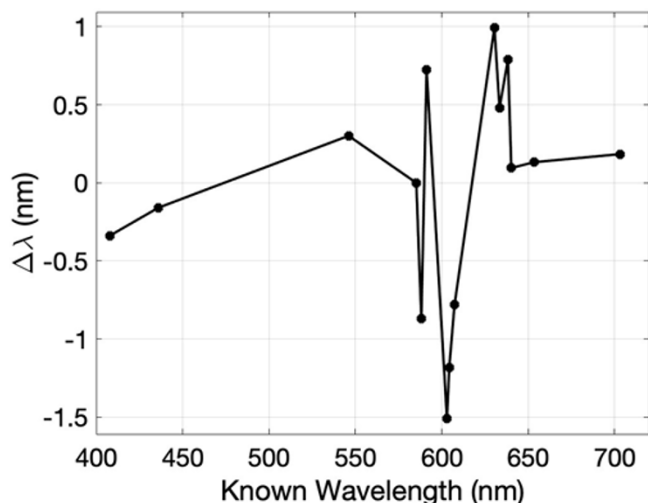


Figure 4. Deviation between known and measured wavelengths in Table 2.

- **Spectral Dimension (X-axis):** Light emitted from the plasma enters the spectrometer, where it is dispersed by a diffraction grating. This dispersion spreads the light across the horizontal axis of the ICCD, so that each of the 1024 columns corresponds to a specific wavelength. This allows for the identification of emission lines from plasma species.
- **Spatial Dimension (Y-axis):** The entrance slit of the spectrometer is aligned with the longitudinal axis of the capillary, enabling light from different axial positions of the plasma to pass through the slit at different vertical positions. These are then mapped onto the 255 rows of the ICCD. Thus, each row corresponds to a unique position along the length of the capillary, preserving the spatial distribution of the emission.
- **Spectral Calibration:**

The spectral calibration maps the horizontal pixel position to the corresponding wavelength. The calibration factor is determined by dividing the total wavelength range covered by the grating by the number of horizontal pixels. For the available diffraction gratings:

$$1200 \text{ g/mm} \rightarrow \text{Conversion Factor} \left(\frac{\text{nm}}{\text{pixel}} \right) = \frac{60}{1024}, \quad (5)$$

$$2400 \text{ g/mm} \rightarrow \text{Conversion Factor} \left(\frac{\text{nm}}{\text{pixel}} \right) = \frac{30}{1024}. \quad (6)$$

These values provide a global wavelength calibration that enables an accurate mapping of the emission lines.

- **Spatial Calibration:**

The spatial calibration converts vertical pixel positions to real distances along the capillary. Assuming a capillary length $L_{\text{capillary}}$, the conversion factor is:

$$\text{Conversion Factor} \left(\frac{\text{mm}}{\text{pixel}} \right) = \frac{L_{\text{capillary}}}{255}. \quad (7)$$

This allows each row of the ICCD image to be associated with a specific longitudinal position in the plasma.

Once both in situ calibrations have been completed and the corresponding factors have been determined, they are applied

across the entire ICCD dataset. This enables a precise mapping of each pixel to its associated wavelength and longitudinal position, allowing for the extraction of spatially resolved plasma parameters. This approach is proposed for future implementation at the I-LUCE facility, as detailed in the spectroscopic setup discussed in Section 3.

Plasma formation and experimental setup

Plasma generation within gas-filled capillaries is achieved by electrical breakdown of the gas, leading to various discharge regimes such as dark, glow, or arc discharges. When a high voltage is applied across electrodes at both ends of the capillary, electrons emitted from the cathode are accelerated by the resulting electric field. These electrons collide with gas atoms, causing ionization and excitation processes that produce free electrons, ions, and photons, culminating in a self-sustaining plasma discharge. Additionally, ion bombardment of the cathode surface leads to secondary electron emission and material sputtering, further influencing the plasma characteristics.

The experimental setup (see Figure 7) for plasma generation in a gas-filled capillary includes a high-voltage system connected to electrodes at both ends, delivering pulsed kilovolt discharges with millisecond durations. Hydrogen gas, produced by electrolysis of water, is introduced into the capillary through mechanically controlled valves operating at repetition rates of 1–10 Hz. The internal pressure is maintained by a regulator to achieve optimal plasma conditions. Plasma initiation is facilitated by a resistor-capacitor (RC) circuit that provides the necessary ionization current.

During the discharge process, the light emitted from the plasma is collected and directed to a spectrometer for spectral dispersion, then recorded by an intensified charge-coupled device (ICCD) camera.

Simultaneously, electrical measurements are performed by monitoring the discharge current through voltage-to-current conversion. All system operations, including gas injection, discharge triggering, and diagnostic measurements, are synchronized by a delay generator.

The optical system enables plasma characterization through OES, with the emitted radiation serving as a diagnostic of local plasma conditions. The capillary configuration with hydrogen plasma offers particular advantages for diagnostics, as it produces strong visible emission lines while minimizing diffraction effects, allowing for accurate determination of electron density and temperature from the spectral features.

Plasma characterization via OES

Spectral analysis of these lines—particularly the Balmer series lines $H\alpha$ (656.3 nm) and $H\beta$ (486.1 nm)—enables reliable electron density characterization via spectral line broadening (SLB) and temperature expectation via their emission energy. These lines are favored for their strong intensity, high signal-to-noise ratio (SNR), minimal spectral overlap, and the availability of extensive empirical data sets (Ref. 2). By analysing the broadening of hydrogen emission lines, particularly $H\alpha$ and $H\beta$, we can probe the behaviour of free electrons in the plasma, enabling diagnostics of electron density and the electric field near emitters. Although free electrons do not emit discrete spectral lines (their radiation is continuous, e.g. bremsstrahlung), their role as perturbs is critical.

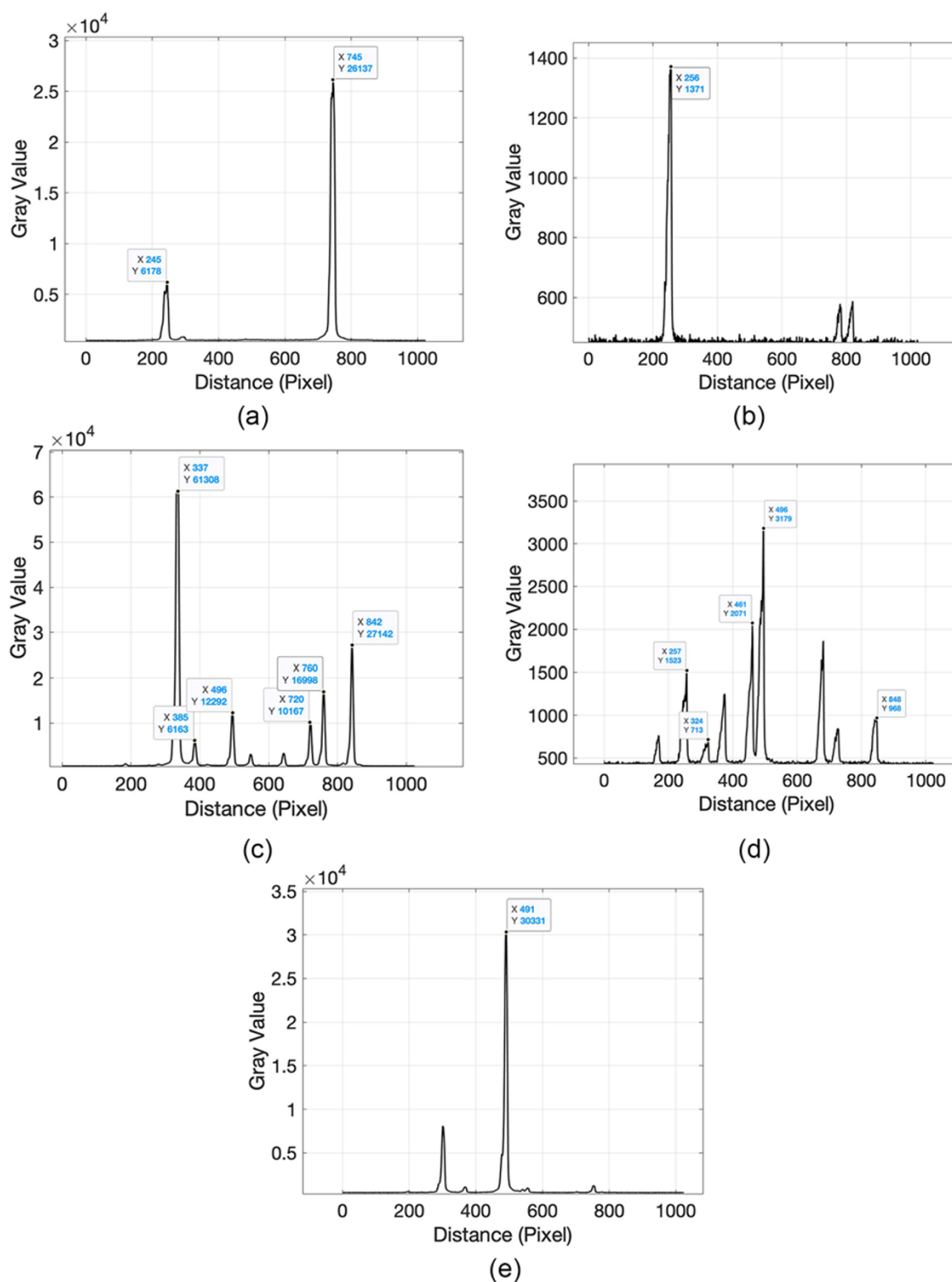


Figure 5. Raw spectral data from 5 intervals showing identified emission lines (Figure 3) and their corresponding pixel positions. (a) Interval 1, (b) Interval 2, (c) Interval 3, (d) Interval 4, (e) Interval 5.

Their high mobility and density induce rapid electric field fluctuations around emitting species, leading to measurable spectral broadening. SLB in plasma arises from several effects (Ref. 12):

- *Natural* broadening – finite lifetime of excited states,
- *Doppler* broadening – thermal motion of emitting particles,
- *Stark* broadening – electric fields from charged particles,
- *Quasi-static* broadening – slowly varying ion fields,
- *Impact or collisional* broadening – frequent particle collisions.

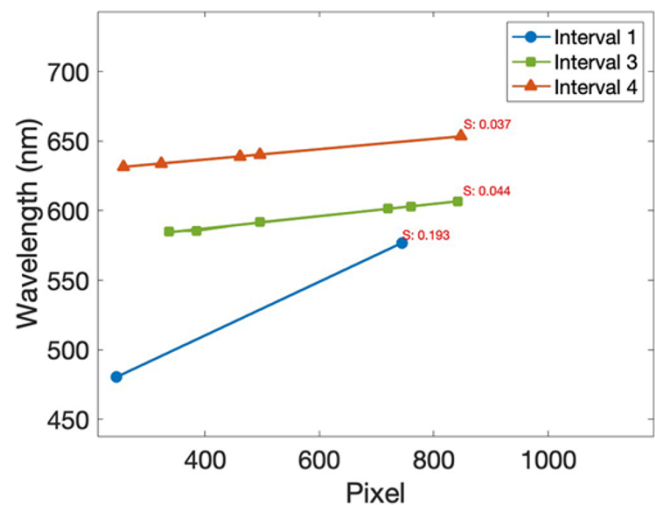


Figure 6. Linear regression of wavelengths versus pixel positions across three spectral intervals (1, 3, 4).

The dominant mechanism depends on plasma conditions (Ref. 13). Doppler broadening results in a Gaussian profile and originates from the motion of emitters – typically heavier species like ions or neutrals. Notably, electrons do not contribute to Doppler broadening, as they do not serve as emitters in this context. Instead, Stark and collisional broadening produce Lorentzian line shapes. When both Gaussian and Lorentzian contributions are present, the overall line profile is described by a Voigt function.

To illustrate this, several theoretical line-shape distributions were compared with experimental data, as shown in (Ref. 14). Figure 8 presents a comparison of the three line-shape models–Gaussian, Lorentzian, and Voigt–fitted to the experimental H β line. Firstly, the data show two close peaks, which could stem from fine-structure splitting in H β . However, that splitting is only 0.016

nm-far below the instrument’s 0.1 nm resolution and further blurred by Stark broadening – so it is negligible.

The Lorentzian fit shows broader wings compared to the Gaussian and aligns more closely with the experimental data in these outer regions. While it slightly deviates at the peak, it provides a better overall match to the wings, suggesting that pressure broadening dominates under these plasma conditions. The Gaussian fit fails to capture the wings and tails, sharply dropping off and underestimating the experimental data in those regions. Although its symmetric bell-shaped form aligns reasonably well in the centre, it does not reproduce the broader features, especially on the left wing. The Voigt profile, which theoretically combines Doppler and pressure broadening effects, shows a reasonably good fit similar to the Lorentzian. However, in this case, it slightly overestimates the peak amplitude and deviates from the experimental points in both the core and wings, suggesting that the Lorentzian component is more representative of the actual broadening mechanism.

We evaluated the goodness of fit using two metrics: the sum of squared errors (SSE), which measures the total squared difference between observed and modelled values, and R-squared (R^2), the coefficient of determination that quantifies the proportion of the data’s variance explained by the model (ranging from 0 to 1). A high R^2 and low SSE indicate a better model agreement. As shown in Table 3, the Lorentzian and Voigt profiles significantly outperform the Gaussian fit. Specifically, the Lorentzian model achieves the highest R^2 (0.96) and the lowest SSE ($2.27e+8$), making it the most suitable for deriving the plasma electron distribution and interpreting the line broadening.

This comparison supports our conclusion that Stark broadening is the dominant mechanism, with a negligible Doppler effect (Ref. 14). This line-broadening analysis is a crucial extension of established methods for measuring electron temperature and density.

Thus, in low-pressure plasmas, such as those produced in our discharge capillaries, Stark broadening – also known as the *Stark–Lo Surdo effect* – is typically the dominant broadening mechanism. It is particularly sensitive to the density and dynamics of

Table 2. Emission lines from Hg/Ne-Ar lamps across five intervals with pixel positions, known wavelengths, and measurement deviations

Interval	Pixel (px)	Measured λ (nm)	known λ (nm)	$\Delta\lambda$ (nm)	Lamp
1	245	407.4450	407.7840	−0.3	Hg
1	745	435.6730	435.8330	−0.1	Hg
2	256	546.3760	546.0750	+0.3	Hg
3	337	585.2490	585.2490	0	Ne
3	385	585.3210	588.1890	−0.8	Ne
3	496	591.9310	591.2080	+0.7	Ar
3	720	601.4900	602.9990	−1.5	Ne
3	760	603.1400	604.3220	−1.1	Ar
3	842	606.6080	607.3880	−0.7	Ne
4	257	631.4720	630.4790	+0.9	Ne
4	324	633.9240	633.4430	+0.4	Ne
4	461	639.0870	638.2990	+0.7	Ne
4	496	640.3500	640.2550	+0.09	Ne
4	848	653.4200	653.2880	+0.1	Ne
5	491	703.4250	703.2410	+0.1	Ne

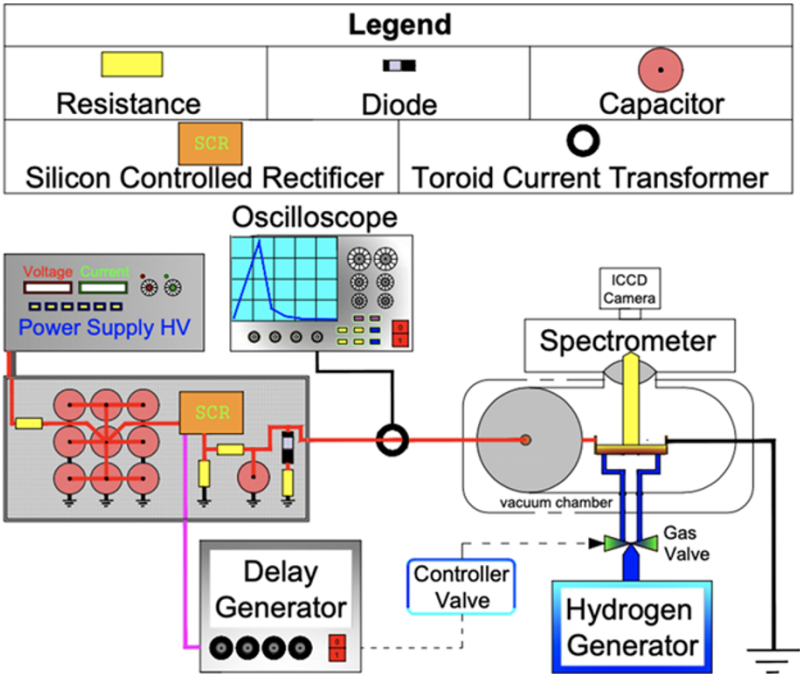


Figure 7. Experimental setup for plasma discharge system and OES diagnostics.

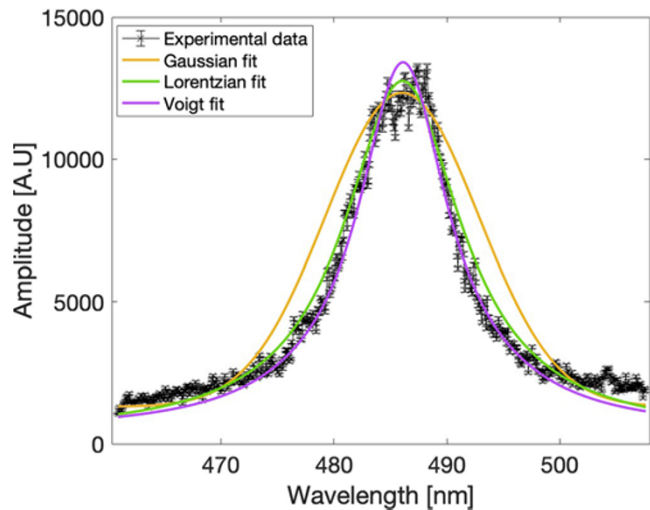


Figure 8. Comparison of Gaussian, Lorentzian, and Voigt line shapes for H_{β} line (Ref. 14)(CC BY-SA 4.0).

Table 3. Goodness of fit for H_{β} profile. R^2 and SSE values comparing Gaussian, Lorentzian, and Voigt fits to the H_{β} line

Fit	SSE	R^2
Gaussian	1.03e+9	0.85
Lorentzian	2.27e+8	0.96
Voigt	4.57e+8	0.93

free electrons, making it a robust tool for diagnostics. Theoretical treatments of Stark broadening incorporate effects such as Debye shielding, ion dynamics, and the motion of the emitters themselves (Refs 15, 16).

The theoretical framework for Stark broadening analysis has evolved through successive refinements, improving diagnostic accuracy. Foundational work established the modern paradigm through Stark broadening tables (SBT), employing the quasi-static approximation for ion microfields, impact approximation for electron microfields and decoupled treatment of field interactions (Ref. 15). These tables enabled robust electron density determination via full width at half maximum (FWHM) measurements of hydrogen lines, a methodology validated by later studies (Refs 15, 16, 17). The FWHM remains the standard metric due to its direct physical interpretation and experimental accessibility.

Computational advancements led to improved Stark broadening models, with numerical simulations overcoming limitations of analytical approximations through self-consistent field calculations and enhanced line profile resolution (Ref. 16).

Further developments introduced the full width at half area (FWHA) parameter, demonstrating superior performance in low-density regimes (Ref. 19). Recent work has refined these methods by addressing systematic biases, yielding improved metrics such as the half-halfwidth at half area (HHWA) (Ref. 20).

The choice of spectral line for plasma diagnostics is critical, as different emission lines provide distinct insights into plasma parameters. Line intensity ratios serve as reliable indicators of electron temperature, while Stark-broadened line widths correlate with electron density. Additionally, the full spectral profile reveals underlying plasma processes. Among the Balmer series, H_{β} has been widely adopted as the most robust diagnostic line, offering reliable density measurements in both low ($\leq 10^{15} \text{ cm}^{-3}$) and high ($10^{17} - 10^{18} \text{ cm}^{-3}$) density regimes, with its capability to determine electron density with $\pm 7\%$ accuracy (Ref. 21). However, at high electron densities ($\geq 10^{18} \text{ cm}^{-3}$), H_{β} becomes broad (Ref. 15), leading to spectral overlap with nearby lines and continuum blending, which complicates accurate measurement.

In such high-density scenarios, H_{α} presents a viable alternative due to its narrower profile – typically four times narrower

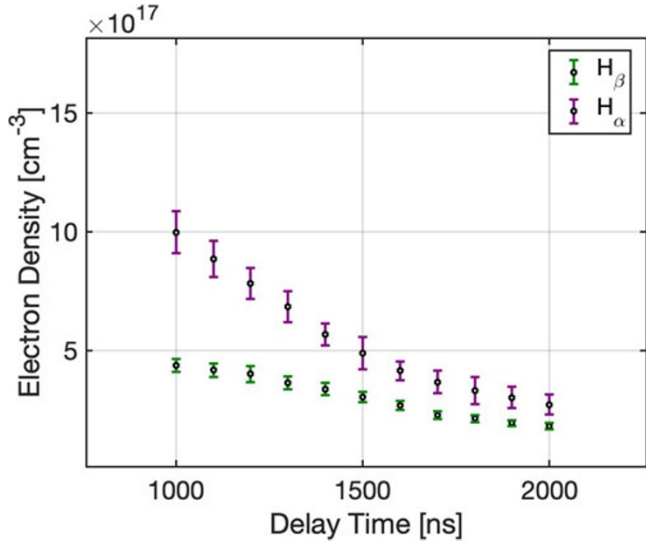


Figure 9. Retrieved electron density from $H\alpha$ and $H\beta$ line as a function of time in a 3 cm length/1 mm diameter capillary (Ref. 2) (CC BY-SA 4.0).

than $H\beta$ under identical conditions – and its higher intensity, which improves the SNR. Historically, $H\alpha$ has been less favoured due to challenges such as self-absorption effects and discrepancies between theoretical and experimental results at low densities ($\leq 10^{15} \text{ cm}^{-3}$) (Ref. 22). Meanwhile, $H\gamma$ has been shown to match $H\beta$'s accuracy at low densities ($\leq 10^{15} \text{ cm}^{-3}$) (Ref. 20), but remains less commonly used due to its weaker emission intensity. The selection between $H\alpha$ and $H\beta$ ultimately depends on the target density range, instrumental resolution, and required precision, with $H\beta$ remaining the standard for general applications while $H\alpha$ gains traction in extreme-density plasmas.

The interest of this work Stark broadening of hydrogen spectral lines by Griem theory, which the FWHM, $\Delta\lambda_{1/2}$, of the Stark-broadened line is directly related to the local electron density and can be extracted using empirical models and tabulated data (Ref. 23):

$$n_e [\text{cm}^{-3}] = 8.02 \times 10^{12} \left[\frac{\Delta\lambda_{1/2}}{\alpha_{1/2}} \right]^{\frac{3}{2}}, \quad (8)$$

where $\alpha_{1/2}$ is a line-broadening parameter (fractional intensity width) that depends on both electron density and electron temperature. It is widely tabulated in the literature for hydrogen Balmer lines (Ref. 15). Electron densities in the range of 10^{17} – 10^{19} cm^{-3} are typically associated with temperatures below 10 eV. For example, at a density of 10^{17} cm^{-3} and a corresponding temperature range of 1–4 eV, $\alpha_{1/2}$ ranges from 0.00186 to 0.00158 nm for the $H\alpha$ line and from 0.00851 to 0.00927 nm for the $H\beta$ line (Ref. 15). This is particularly valid in our case, where the plasma is emitted in the visible range and operates at temperatures of approximately 1–4 eV, allowing other broadening mechanisms to be neglected.

Figure 9 shows the evolution of the electron density (n_e) as a function of plasma recombination time, derived from $H\alpha$ and $H\beta$ line measurements under 12 kV, 400 A discharge, as reported in (Ref. 2).

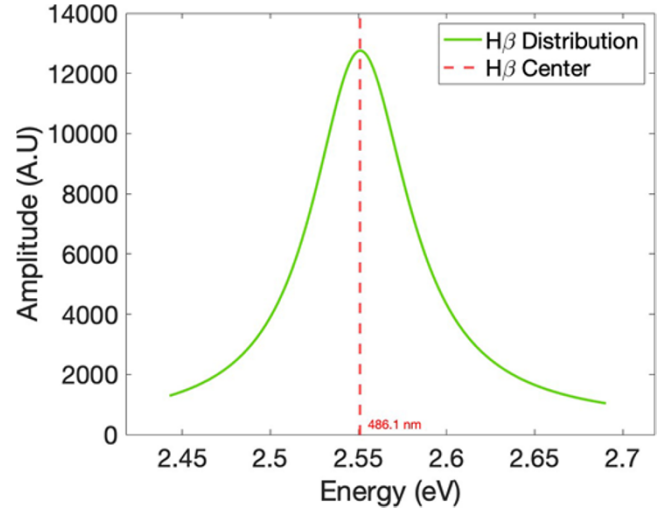


Figure 10. Photon energy of $H\beta$ line with Lorentzian fit converted from Figure 8.

A notable difference is observed between the plasma densities measured from the $H\alpha$ and $H\beta$ lines, with the $H\alpha$ -based measurement yielding values nearly twice as high. This variation can be attributed to the intrinsic characteristics of the $H\alpha$ line, such as its increased sensitivity to self-absorption and its relatively higher signal strength (Ref. 16). Self-absorption means that some emitted photons are re-absorbed by the plasma before escaping. While this makes the line easier to detect, it can also result in an artificially higher density estimate. In contrast, the $H\beta$ line, being less affected by these factors because it is at a shorter wavelength and has a lower transition probability – so its line is more optically thin and more reliable for actual plasma density. In our case, $H\alpha$ (higher opacity) is absorbed more than $H\beta$ thus the observed $H\alpha/H\beta$ ratio decreases which $H\alpha$ is absorbed 2 times more than $H\beta$, then the ratio drops by ~ 30 –50%. This can reveal that we have moderate self-absorption and still have an optically thin plasma.

Emission lines also provide valuable information on line intensities, which are governed by plasma thermodynamics. For example, the $H\beta$ line (486.1 nm, 2.55 eV) arises from hydrogen transitions from $n = 4$ to $n = 2$. This is illustrated in Figure 10, which is derived from the spectral data presented in Figure 8.

Although the transition energy is fixed, the line intensity depends on the electron temperature due to the ionization-recombination equilibrium. The Saha equation quantitatively relates T_e to the ionization state:

$$\frac{n_e n_p}{n_H} = \left(\frac{2\pi m_e k_B T}{h^2} \right)^{\frac{3}{2}} \exp \left(-\frac{E_H}{k_B T} \right), \quad (9)$$

where n_H : neutral hydrogen density, n_p : proton density, n_e : electron density, m_e : electron mass, T : absolute temperature (K), k_B : Boltzmann constant, h : Planck constant, E_H : hydrogen ionization energy (13.6 eV).

This reveals three temperature regimes for $H\beta$ emission. From Equation 9, we can observe that at low temperatures (e.g. below 8,000 K or 0.68 eV), the exponential term ($\exp(-\frac{E_H}{k_B T}) \ll 1$) maintains hydrogen neutrality ($n_H \gg n_p$), quenching the recombination of emission.

As the temperature increases ($8,000 \text{ K} \leq T_e \leq 15,000 \text{ K}$), optimal $H\beta$ production as partial ionization ($n_p \sim n_H$) enables efficient recombination:

Table 4. Considered critical density (n_c) for H_α and H_β lines

Line	State	Transition	γ (cm ³)	A (s ⁻¹)	n_c (cm ⁻³)
H_α	3	3 \leftarrow 2	$\sim 10^{-8}$	4.41×10^7	4.41×10^{15}
H_β	4	4 \leftarrow 2	$\sim 10^{-8}$	8.41×10^6	8.41×10^{14}

$$\epsilon_{H_\beta} \propto n_e n_p \alpha H_\beta^{\text{eff}}(T_e), \quad (10)$$

where $\alpha H_\beta^{\text{eff}}$ is the temperature-dependent effective recombination coefficient. Then at $T_e > 15,000$ K (1.29 eV), hydrogen becomes significantly ionized, or reaches near-complete ionization ($n_H \leftarrow 0$) depletes recombination targets, diminishing H_β .

However, determining the electron temperature in capillary discharges can be approached through various methods, including detailed plasma modelling. For rapid estimation, in capillary discharges, the peak on-axis electron temperature can be estimated using a simplified model that balances electron thermal conductivity and Joule heating. This approach yields a scaling law for the electron temperature:

$$T_e [\text{eV}] = 5.7 \left[\frac{I}{r_{\text{cap}}} \right]^{\frac{2}{5}}. \quad (11)$$

Here, I (kV) is the discharge current measured from the oscilloscope, and r_{cap} (mm) is the capillary radius (Refs 24, 25). For a discharge current of 0.4 kA and a capillary radius of 0.5 mm (Ref. 2), this formula predicts an on-axis electron temperature of ~ 5.2 eV. At this temperature, electrons possess sufficient energy to fully ionize hydrogen, supporting the formation of a plasma channel. This method assumes that the plasma approaches a quasi-static model (QSM), which is particularly useful for understanding the dynamics in capillary discharge plasmas.

While the QSM offers a useful initial estimate, it simplifies plasma dynamics by neglecting temporal variations, cooling effects, and recombination. Nevertheless, it serves as a practical tool for assessing whether plasma conditions are suitable for full ionization and aids in the design and diagnostics of plasma-based accelerators. The actual plasma formation process occurs through distinct evolutionary stages (Ref. 26).

Following discharge initiation, the system progresses from initial ionization through thermal conduction build-up before reaching full ionization. Only in the subsequent phase does the plasma approach a quasi-steady state with characteristic parabolic electron density profiles, featuring a central temperature maximum and density minimum.

However, the QSM remains an idealized approximation. It assumes axial uniformity and neglects energy losses, spatial gradients, and time-dependent effects. As a result, it tends to overestimate the maximum temperature, particularly in the early discharge phases before thermal equilibrium is established. The predicted value represents an upper limit rather than an average, as it does not account for recombination, cooling, or axial inhomogeneities. Despite these simplifications, the model's predictive capability offers a valuable theoretical benchmark. Our experimental measurements aim to quantify the deviation between this idealized prediction and observed plasma conditions, particularly during the critical transition to full ionization.

To end this, to determine the electron temperature (T_e) in our hydrogen plasma discharge, we employ population models that

account for excitation and de-excitation processes. The choice of model depends on the plasma density and dominant processes, with three primary models:

- *Corona*: Applicable to low-density plasmas where radiative processes dominate,
- *Local thermodynamic equilibrium (LTE)*: Valid for high-density plasmas where collisional processes thermalize level population,
- *Collisional-radiative (CR)*: Bridges the gap between corona and LTE regimes, accounting for both collisional and radiative processes.

For our hydrogen plasma with $n_e \approx 10^{17}$ cm⁻³ (see Figure 9) and T_e expected between 1 and 4 eV from Griem's theory, we first assess whether the LTE conditions hold. The LTE criterion requires n_e to exceed the critical density n_c^{LTE} , which is the density at which the collisional de-excitation rate equals the radiative decay rate for a given transition:

$$n_c^{\text{LTE}} \gtrsim 10^{16} \text{ cm}^{-3} \times \left(\frac{T_e}{10^4 \text{ K}} \right)^{\frac{1}{2}}. \quad (12)$$

For T_e of 1–4 eV, n_c varies from 1.08×10^{16} to 2.16×10^{16} cm⁻³. Given that our plasma's electron density is 10^{17} cm⁻³, which exceeds this threshold, it suggests that LTE is plausible.

A stricter validation involves comparing n_e with the critical density (n_c) for specific transitions, where collisional de-excitation balances radiative decay:

$$n_c [\text{cm}^{-3}] = \frac{A_{ul}}{\gamma_{ul}}, \quad (13)$$

with A_{ul} s⁻¹ as the Einstein coefficient and γ_{ul} (cm³) as the collisional de-excitation rate coefficient (Ref. 14). As shown in Table 4, the critical densities for the hydrogen lines are significantly lower than our measured electron density, confirming that collisional processes dominate.

Furthermore, the widely used McWhirter criterion provides a stricter check for LTE validity, which establishes the minimum electron density required to ensure that collisional processes dominate over radiative processes (Ref. 27):

$$n_e [\text{cm}^{-3}] \geq 1.6 \times 10^{12} T_e^{\frac{1}{2}} (\Delta E)^3, \quad (14)$$

where ΔE is the energy gap between the upper and lower levels of the transition. The ΔE between hydrogen energy levels is crucial because it directly influences the rates of collisional excitation and de-excitation processes.

A larger ΔE corresponds to a lower probability of collisional excitation, necessitating a higher electron density to achieve LTE. For the H_α and H_β transitions, the values of ΔE are ≈ 1.9 and 2.55 eV, respectively. At electron temperatures of 1–4 eV, the minimum electron densities required to maintain LTE are the following:

- $H\alpha: \approx 1.09 \times 10^{13}$ to $2.19 \times 10^{13} \text{ cm}^{-3}$,
- $H\beta: \approx 2.65 \times 10^{13}$ to $5.31 \times 10^{13} \text{ cm}^{-3}$.

Lastly, the $H\alpha/H\beta$ ratio known as the Balmer decrement is used to assess whether the LTE conditions are satisfied. This ratio reflects the balance between collisional and radiative processes that govern the excitation and de-excitation of hydrogen atoms. To evaluate this, we begin by converting level populations into line intensities and then calculate the $H\alpha/H\beta$ intensity ratio. The intensity of an emission line is directly related to the population of the upper energy level involved in the transition. This relationship is given by:

$$I_{ul} \propto n_u \cdot A_{ul} \cdot h\nu, \quad (15)$$

where I_{ul} : transition intensity of upper level u to lower level l , n_u : population density of the upper level, A_{ul} : Einstein coefficient (probability of emission), h : Planck's constant, ν : frequency of the emitted light.

Applying this to the lines $H\alpha$ (transition from $n = 3$ to $n = 2$) and $H\beta$ (transition from $n = 4$ to $n = 2$):

$$\frac{I_{H\alpha}}{I_{H\beta}} = \frac{n_3 \cdot A_{32} \cdot \nu_{32}}{n_4 \cdot A_{42} \cdot \nu_{42}}. \quad (16)$$

The population densities n_2 and n_4 can be related using the Boltzmann distribution:

$$\frac{n_3}{n_4} = \frac{g_3}{g_4} \cdot \exp\left(-\frac{E_3 - E_4}{k_B T_e}\right), \quad (17)$$

where $g_n = 2n^2$: the statistical weight of level n , $E_n = -13.6 \frac{\text{eV}}{n^2}$: energy of level n , k_B : Boltzmann constant, T_e : electron temperature.

Substituting Equation 17 into Equation 16, we obtain the final expression for the $H\alpha/H\beta$ ratio:

$$\frac{I_{H\alpha}}{I_{H\beta}} = \left(\frac{g_3}{g_4} \cdot \exp\left(-\frac{E_3 - E_4}{k_B T_e}\right)\right) \cdot \left(\frac{A_{32} \cdot \nu_{32}}{A_{42} \cdot \nu_{42}}\right). \quad (18)$$

Figure 11 illustrates the time-dependent $H\alpha/H\beta$ ratio. In our observations, the $H\alpha/H\beta$ ratio fluctuates between 0.5 and approximately 1, suggesting that the plasma is optically thin and predominantly influenced by collisional excitation, characteristic of Case A conditions. Such low ratios indicate that collisional processes dominate and that the plasma maintains LTE. In contrast, under Case B conditions, where radiative recombination prevails, the $H\alpha/H\beta$ ratio typically approaches or exceeds 2.86, as established by recombination theory (Ref. 28).

Having confirmed that the plasma satisfies LTE conditions, we can proceed to estimate the T_e using LTE-based diagnostics. Under LTE the T_e can be determined by analysing the $H\alpha/H\beta$ intensity ratio, as previously discussed. Alternatively, it can be estimated by comparing the intensities of spectral lines from different ionization states of the same element (e.g. O II and O III), provided that the plasma density is known (Ref. 15).

Focusing on the first approach, with the electron density and $H\alpha/H\beta$ ratio determined, rearrange the Boltzmann equation to

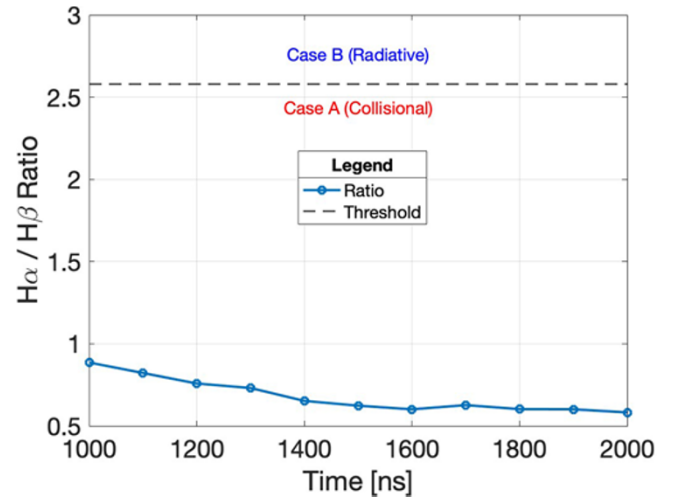


Figure 11. $H\alpha/H\beta$ ratio as a function of time. The dashed line marks the theoretical threshold value.

solve for the electron temperature:

$$\frac{n_u}{n_l} = \frac{g_u}{g_l} \cdot \exp\left(-\frac{E_u - E_l}{k_B T_e}\right), \quad (19)$$

which can be rearranged to:

$$T_e = \frac{E_u - E_l}{k_B \left[\ln\left(\frac{g_l}{g_u} \cdot \frac{n_u}{n_l}\right) \right]}. \quad (20)$$

Here, $E_u - E_l$ is the excitation energy required to excite an electron from the lower energy level l to the upper level u . By substituting the known values for the energy levels and statistical weights, and using the measured intensity ratio to determine $\frac{n_u}{n_l}$, we can calculate the electron temperature. All relevant parameters can be obtained from the NIST database (Ref. 11) by selecting the desired spectral line. Table 5 summarizes the atomic parameters relevant to the $H\alpha$ and $H\beta$ lines.

The electron temperature derived from the $H\alpha/H\beta$ intensity ratio is presented in Figure 12.

The observed electron temperature ranges from approximately 0.9 to 5 eV, which extends beyond the typical expected range of 1–4 eV for such plasmas.

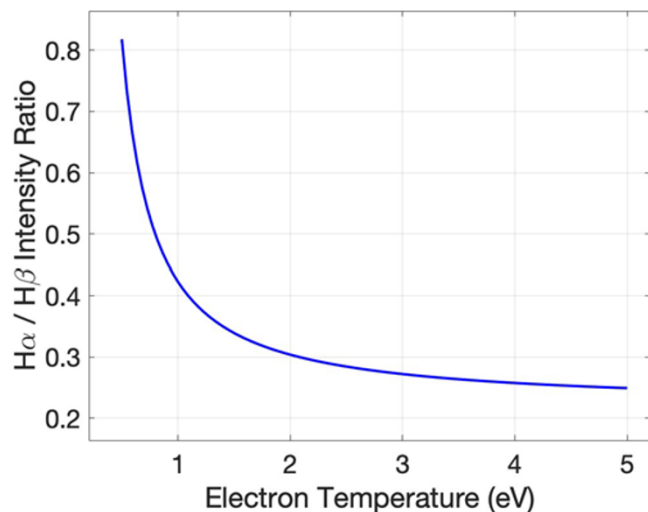
The deviation in the $H\alpha/H\beta$ -derived electron temperature can be attributed to several factors, with self-absorption being a primary contributor. This phenomenon occurs when emitted $H\alpha$ photons are reabsorbed by cooler plasma regions along the line of sight, distorting the observed line profile and artificially altering the $H\alpha/H\beta$ ratio, leading to inaccurate temperature estimations.

Additionally, different emission lines respond uniquely to local plasma conditions because of variations in excitation and recombination processes. The $H\alpha$ and $H\beta$ lines, being recombination lines, are particularly sensitive to cooler plasma zones where recombination dominates. Consequently, their emission is biased toward these regions, skewing the inferred temperature toward an average that may not represent the entire plasma.

For more robust diagnostics, collisionally excited lines, such as O II and O III are preferable. These lines are less susceptible to self-absorption because they originate in ionized regions with lower

Table 5. Atomic parameters for H_{α} and H_{β}

Line	State	Transition	g	A (s^{-1})	λ (nm)	E (eV)
H_{β}	4	$4 \leftarrow 2$	$2n^2 = 32$	8.410×10^6	486.1	1.89
H_{α}	3	$3 \leftarrow 2$	$2n^2 = 18$	4.410×10^7	656.3	2.55

**Figure 12.** Retrieved electron temperature from H_{α}/H_{β} ratio.

optical depths compared to H_{α} . Moreover, since their excitation depends directly on electron collisions, they provide a more reliable measure of the local electron temperature in their respective ionized zones.

An alternative diagnostic approach involves analysing spectral line intensity ratios of the same ion. However, the minimal differences in excitation energies and inherent theoretical uncertainties limit the precision of temperature measurements using single-ion line ratios. For dense plasmas in LTE conditions, a more robust technique involves analysing intensity ratios between successive ionization states (e.g. O II/O III or N II/N III). This method capitalizes on the more pronounced temperature sensitivity of the ionization equilibrium, yielding more accurate diagnostics. The diagnostic power of this approach stems from its independent determination of plasma parameters: electron density from H_{α} or H_{β} line broadening and electron temperature from O II/O III line ratios. This separation ensures that temperature measurements remain unaffected by H_{α} self-absorption effects. The intensity ratio method thus provides a valuable complement to H_{α}/H_{β} diagnostics, especially in regions where recombination processes may distort measurements, given as (Ref. 15):

$$R = \frac{\lambda_2^3 f_2 g_2}{\lambda_1^3 f_1 g_1} \left(4\pi^2 a_0^3 n_e \right)^{-1} \left(\frac{T_e}{E_H} \right)^{\left(\frac{3}{2} \right)} \times \exp \left(-\frac{E_2 + E_{\infty} - E_1 - \Delta E_{\infty}}{T_e} \right), \quad (21)$$

where a_0 : Bohr radius, g : statistical weight, λ : spectral line wavelength, f : absorption oscillator strength, E : spectral line excitation energy, E_H : hydrogen ionization energy, E_{∞} : lower stage ionization energy, ΔE_{∞} : correction factor (ionization energy reduction or shift to E_{∞}).

Table 6. Correction factor (ΔE_{∞}) for H_{α} and H_{β} lines as a function of time

Time (ns)	H_{α} : ΔE_{∞} (eV)	H_{β} : ΔE_{∞} (eV)
1000	0.696	0.528
1100	0.6695	0.521
1200	0.642	0.513
1300	0.614	0.497
1400	0.577	0.485
1500	0.548	0.468
1600	0.5194	0.449
1700	0.499	0.425
1800	0.482	0.416
1900	0.467	0.404
2000	0.452	0.395

The parameters with subscripts 1 and 2 correspond to the lower and upper energy levels of the transition, respectively. To identify additional ions present in a hydrogen plasma, it is useful to analyse the emission spectrum while considering the capillary material. Understanding the chemical composition is essential because elements of the capillary can be introduced into the plasma. For example, VeroClear, a material similar to polymethyl methacrylate (PMMA), commonly known as acrylic, contains carbon and oxygen ($C_5O_2H_8$), which may be released into the plasma during processing. These elements can contribute to observed spectral lines through excitation and emission processes, as reported in (Ref. 29). Some lines may be more prominent in cooler regions, while others become significant at higher temperatures, even within the same physical location in the plasma.

Using the electron density values determined from each line as reported in Figure 9, and applying the subsequent ionization stage method described earlier, we calculated the correction factor (CF) for the H_{α} and H_{β} lines. All relevant atomic data were taken from (Ref. 29). Table 6 presents the corresponding plasma parameters derived at different times.

By analysing the emission lines of singly ionized oxygen (O II at 471.9803 nm) and doubly ionized oxygen (O III at 508.8922 nm), we determined the electron temperature as a function of plasma recombination time, as depicted in Figure 13. All physical constants and spectral data for oxygen ions are taken from (Ref. 29).

The electron temperature exhibits a gradual decline from approximately 2.4 to 2.1 eV, correlating with the plasma's recombination dynamics. Both spectral lines display consistent downward trends, aligning with the observed decrease in electron density. However, minor discrepancies between the temperatures derived from O II and O III suggest sensitivity to local plasma conditions or potential line broadening effects, which may affect the precision of these measurements compared to diagnostics utilizing heavier atomic species.

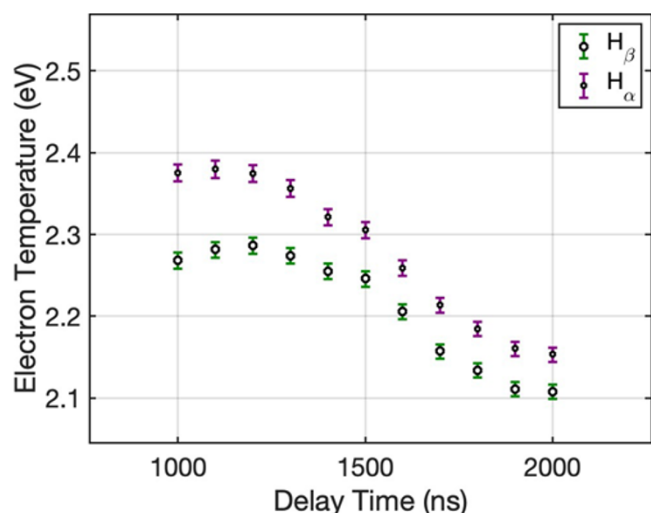


Figure 13. Retrieved plasma electron temperatures, $T_e(\frac{OII}{OIII}(H\alpha))$ and $T_e(\frac{OII}{OIII}(H\beta))$, as a function of time in a 3 cm length/1 mm diameter capillary.

Unlike the $H\alpha$ and $H\beta$ line ratios, which can be influenced by recombination processes at lower temperatures, the electron temperature is more reliably determined from the intensity ratio of the O II/O III lines. These lines, arising from ionization and recombination processes, are less affected by such effects and better reflect the actual plasma temperature.

The intensity ratio between O II and O III, representing different ionization states of oxygen, is primarily governed by electron temperature, making it a more accurate indicator with fewer distortions from plasma conditions. The electron temperature in our plasma reaches a maximum of 2.4 eV, approximately 0.46 times lower than the maximum on-axis temperature achievable along the plasma axis, as reported earlier. Despite this, the plasma maintains sufficiently high electron temperatures to support dominant electron-electron collisions. This is corroborated by Stark broadening measurements, which indicate that electron collisions are the primary broadening mechanism in our plasma. Furthermore, the consistency of these findings with the assumptions of LTE reinforces the validity of our diagnostic techniques and the applicability of LTE to characterize the plasma state. This method aligns well with the expected electron temperature, given the plasma's density, indicating its higher accuracy under LTE conditions.

To further validate the presence of specific ions in the plasma, theoretical simulations based on established databases such as NIST atomic spectra (Ref. 11) can be employed. We consider a VeroClear ($C_5O_2H_8$) capillary – composed of 82% C, 16% O, 1% H and 1% N – with an electron density of $5 \times 10^{17} \text{ cm}^{-3}$ at the $H\alpha$ emission time of 1500 ns (Figure 9), corresponding to 2.3 eV (Figure 13). However, diagnostics based on the $H\alpha/H\beta$ intensity ratio (Figure 12) suggest that the electron temperature may actually range from 0.8 to 5 eV. To ensure that forbidden lines from C I, C II, C III, N I, N II, N III, and O I, O II and O III remain detectable even at this temperature range, we simulate their emission spectra for $T_e = 1 \text{ eV}$ and $T_e = 2 \text{ eV}$ under the same electron density. Figure 14 illustrates the anticipated spectral lines of these ions, showing the individual lines of O II, O III, N II and N III, as well as the cumulative spectrum. The simulations assume the stated plasma conditions – $T_e = 1 \text{ eV}$ (top

panel) and $T_e = 2 \text{ eV}$ (bottom panel), with $5 \times 10^{17} \text{ cm}^{-3}$ – consistent with the density range inferred from $H\alpha$ and $H\beta$ line profiles.

To validate our experimental findings and theoretical expectations, we employed COMSOL Multiphysics (Ref. 30) to model plasma discharge within gas-filled capillaries. This simulation approach, detailed in our previous study, demonstrates strong agreement with both observed data and theoretical predictions (Ref. 31).

Plasma-driven VHEE dosimetry

The integration of plasma diagnostics and LPA technologies aims to produce a stable, ultra-short, and high repetition rate suitable for VHEE (50–250 MeV) applications (Refs 5, 6, 7, 8). These beams are particularly promising for medical applications, particularly in the treatment of deep-seated tumours through advanced radiation therapy (RT) techniques (Ref. 6).

To assess the feasibility of VHEE beams in clinical settings, we performed Monte Carlo (MC) (Ref. 32) simulations using the Geant4 toolkit to evaluate the dose distributions from a $200 \pm 25 \text{ MeV}$ electron beam carrying 120 pC per bunch, generated by a capillary-based LPA system (Ref. 33). These electrons originate from a capillary-LPA system (Ref. 33) – specifically, a 7 mm capillary setup driven by a 150 TW, 25 fs ($\sim 3 \text{ J}$) laser at the Gwangju Institute of Science and Technology (GIST), which produced the desired beam parameters.

In contrast, our work employs the advanced I-LUCE platform featuring a 3 cm capillary. Despite this difference, the GIST laser parameters remain applicable and sufficient to reproduce clinically relevant VHEE beams using typical LPA conditions. We used this experimentally generated, capillary-driven electron beam as the source for our MC simulations, focusing on spatial dose profiles in water phantoms to assess both coverage and conformality. Ultimately, this analysis verifies the potential of LPA-generated VHEE beams to deliver therapeutic doses effectively in clinical scenarios.

Figure 15 illustrates the two-dimensional dose distribution (top panel) and the corresponding transverse dose profile (bottom panel) resulting from four electron beams (each transporting a charge of 120 pC) incident from four orthogonal directions. The average simulated dose per set of four shots resulted to be 0.28 Gy. If each shot can be released at 10 Hz we will have 28 Gy in one second.

With the advent of emerging kHz laser systems, it is conceivable to achieve higher dose fractions in just 100 ms. While the development of high-repetition-rate plasma targets is still in its nascent stages, no fundamental barriers have been identified, and achieving kHz repetition rates appears feasible. Several facilities have already demonstrated the viability of such systems for high-repetition-rate applications (Ref. 33).

In the forthcoming second phase of the I-LUCE facility, plans are underway to upgrade the laser system to operate at 100 Hz, accompanied by enhancements in beam delivery capabilities. This advancement could pave the way for VHEE applications in RT, or ultra-high dose rate (UHDR) application known as FLASH-RT, where doses of $\geq 40 \text{ Gy}$ are typically administered in less than one second.

Using the upgraded I-LUCE laser system and scaling the output to a beam with a 120 pC charge per shot, it is possible to reach dose levels suitable for delivery in the FLASH regime. In addition to increasing the laser's repetition rate, enhancing the charge per

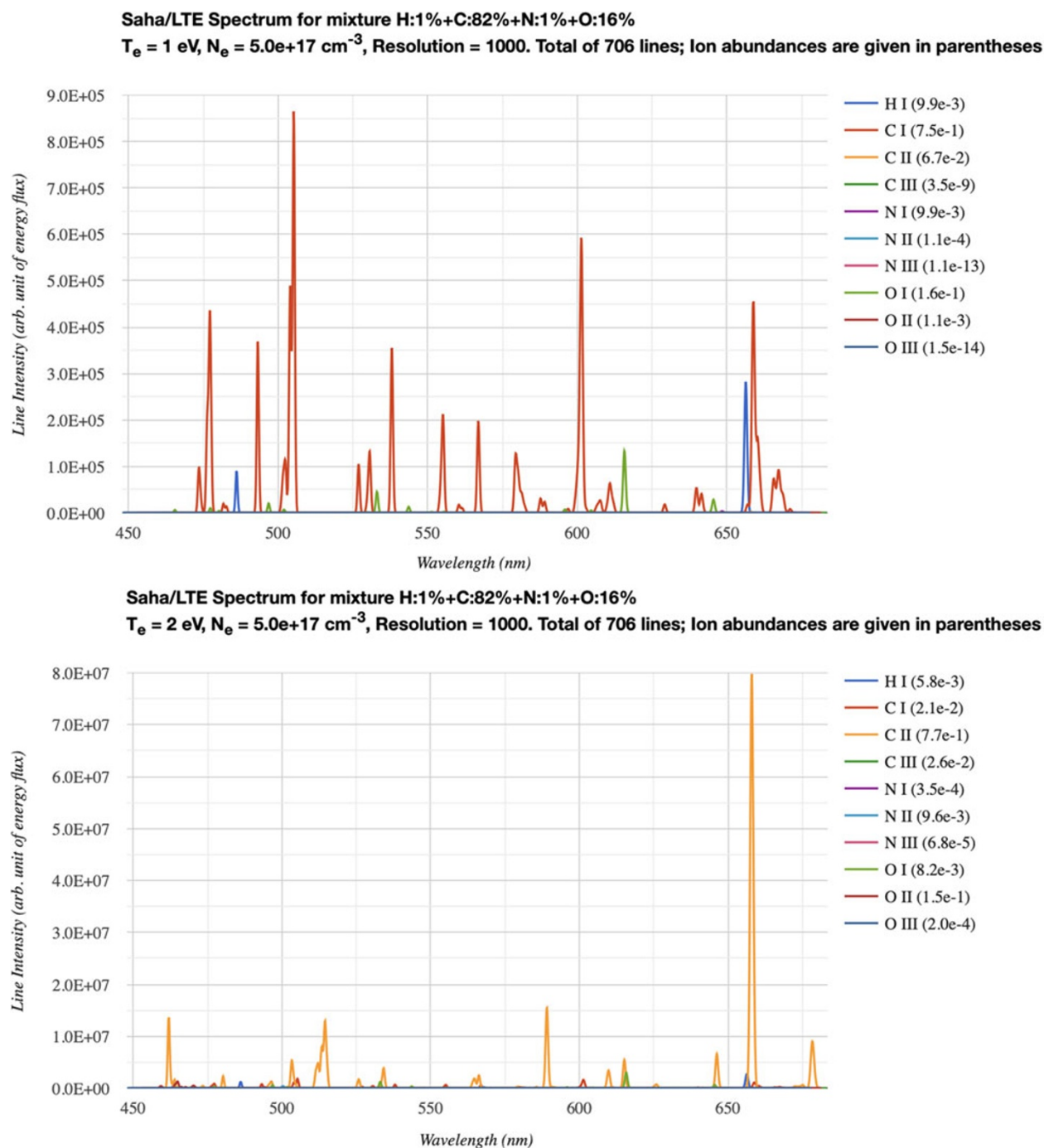


Figure 14. Illustration of the expected spectral lines for O II, O III, N II, N III, C II, and C III at an electron density of $5 \times 10^{17} \text{ cm}^{-3}$, with electron temperatures of 1 eV (top) and 2 eV (bottom), based on NIST database (Ref. 11).

electron bunch offers another avenue to achieve the desired dose rates. However, this approach must be balanced against potential challenges such as emittance growth and beam instabilities, which can affect beam quality.

These developments underscore the potential of LPA-driven VHEE beams to revolutionize cancer therapy, offering precise, high-dose treatments in remarkably short timeframes. The compact nature of LPA systems and their ability to deliver UHDRs make them promising candidates for clinical applications, particularly FLASH-RT.

Conclusion

To ensure precise spectral measurements for plasma diagnostics, we implemented wavelength calibration using Hg/Ne-Ar atomic emission lamps. Time-resolved spectroscopic techniques were employed to characterize the discharge plasmas, enabling the determination of electron density and temperature through SLB methods. Our analysis confirmed that Stark broadening, indicative of collisional interactions, is the dominant broadening mechanism, suggesting the presence of hot electrons within the plasma.

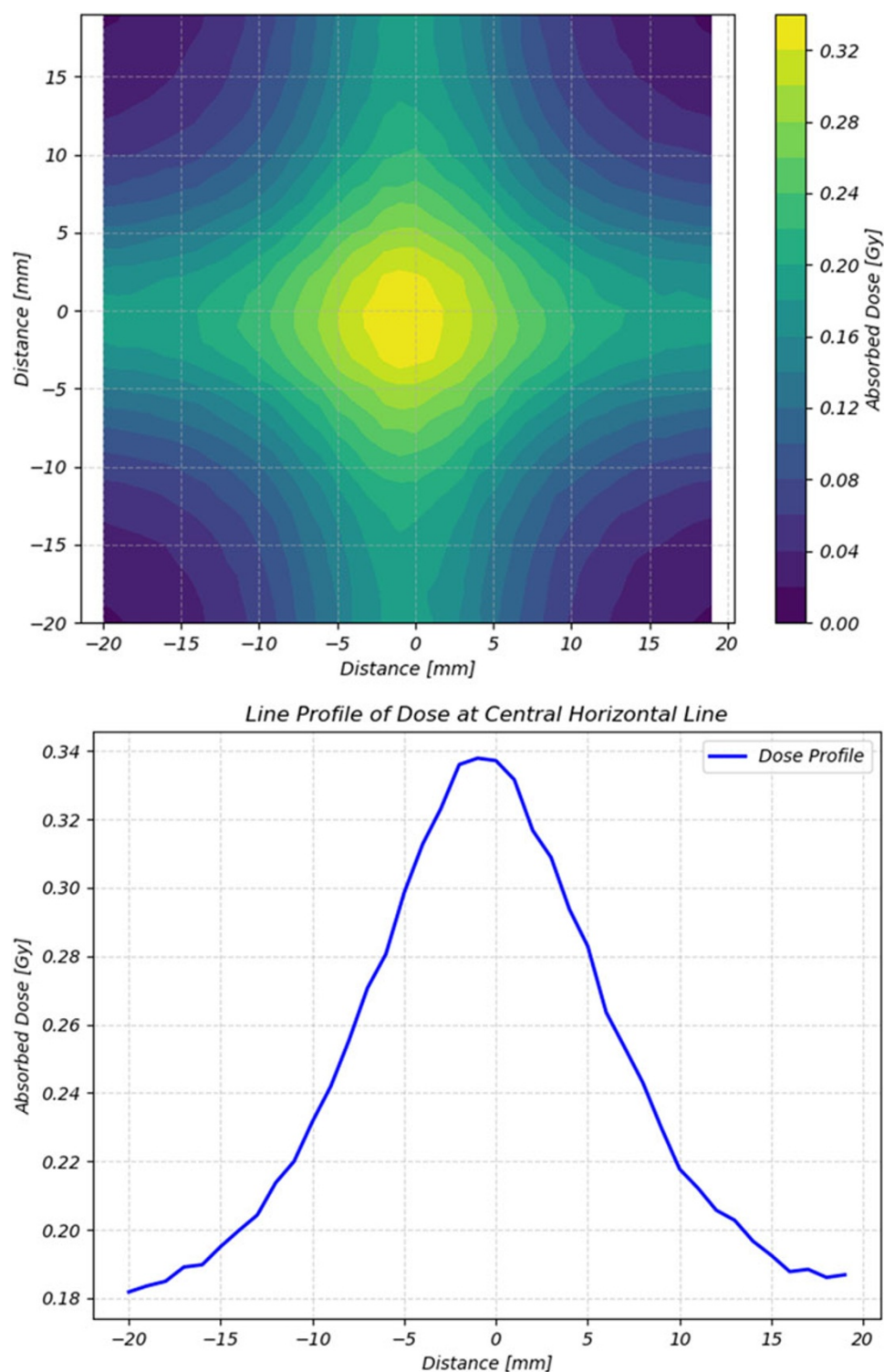


Figure 15. 2D dose distribution of four electron beams (top), and line profile of four along the y axis of the dose distribution (bottom).

The plasma conditions achieved were consistent with LTE, allowing for the application of various diagnostic approaches to determine the electron temperature. Establishing LTE is crucial for LPAs, as it ensures stable and uniform plasma conditions necessary for efficient acceleration processes. We employed a multi-technique spectroscopic approach to accurately characterize the electron density and temperature within the plasma. These diagnostic measurements provide insights into the plasma's properties,

but were not utilized to drive the parameters for the Monte Carlo simulations.

MC simulations were performed independently to evaluate the dose distribution of the VHEE beams, revealing a maximum dose of 0.28 Gy. With advancements in kHz laser systems, this could translate to dose rates of up to 28 Gy per second, highlighting the feasibility of VHEE applications in RT.

Data availability statement. The data supporting this study are not publicly available due to legal or ethical restrictions but can be obtained from the corresponding author upon reasonable request.

Acknowledgements. The authors are deeply grateful to Prof. Danilo Giulietti for his generous insights and thoughtful discussions.

Funding statement. This research was supported by three Italian PNRR (Piano Nazionale di Ripresa e Resilienza) programs-ANTHEM (Advanced Technologies for Human-Centered Medicine, project no. PNC0000003), EUAPS (EuPRAXIA Advanced Photon Sources, project no. IR00000030), both funded by the EU's NextGenerationEU initiative – and SAMOTHRACE (Sicilian Micro and Nano Technology Research and Innovation Center). In particular, the ANTHEM project supports FLASH-RT research by funding the development of laser-driven electron beams to investigate FLASH effects.

Conflicts of interest. The authors declare that there are no conflicts of interest.

Ethical standards. The research meets all ethical guidelines, including adherence to the legal requirements of the study country.

References

1. Tajima T and Dawson JM (1979) Laser electron-accelerator. *Physical Review Letters* **43**(4), 267–270. doi:10.1103/PhysRevLett.43.267.
2. Arjmand S, Anania MP, Biagioni A, Ferrario M, Del Franco M, Galletti M, Lollo V, Pellegrini D, Pompili R and Zigler A (2023) Investigating of plasma diagnostics by utilizing spectroscopic measurements of Balmer emission. *JINST* **18**, C05007. doi:10.1088/1748-0221/18/05/C05007
3. Cirrone GAP, Amato A, Bandieramonte D, Bonanno D, Cantone G, Catalano R, Cuttone G, Maggiore G, Miraglia A, Musumeci M and Passarello D (2023) Ion acceleration by laser-matter interaction: Status and perspective with the upcoming i-LUCE facility at INFN-LNS. In Proceedings of the 14th International Particle Accelerator Conference (IPAC'23), Geneva, Switzerland, 7–12 May 2023 (pp. 4386–4388). Venice, Italy: JACoW Publishing.
4. Cirrone GAP, Arjmand S, Sciuto A, Fattori S, Pappalardo AD, Catalano R, Cuttone G, Oliva D, Petringa G and Tramontana A (2025) Beam delivery methods for laser-driven proton sources. *Nuclear Instruments and Methods in Physics Research A* **1080**, 170715. doi:10.1016/j.nima.2025.170715
5. Arjmand S, Amato A, Catalano R, Cuttone G, Manna C, Oliva D, Pappalardo AD, Petringa G, Suarez J, Vinciguerra F and Cirrone GA (2024) Implementing plasma-discharge capillary design for very high energy electron (VHEE) applications at I-LUCE facility. *RAD Conference Proceedings* **8**, 96–102. doi:10.21175/RadProc.2024.18
6. Labate L, Palla D, Panetta D, Avella F, Baffigi F, Brandi F, Di Martino F, Fulgentini L, Giulietti A, Köster P and Terzani D (2020) Toward an effective use of laser-driven very high energy electrons for radiotherapy: Feasibility assessment of multi-field and intensity modulation irradiation schemes. *Scientific Reports* **10**(1), 17307. doi:10.1038/s41598-020-74256-w
7. Whitmore L, Mackay RI, van Herk M, Jones JK and Jones RM (2021) Focused VHEE (very high energy electron) beams and dose delivery for radiotherapy applications. *Scientific Reports* **11**, 14013. doi:10.1038/s41598-021-93276-8
8. Arjmand S, Amato A, Catalano R, Manna C, Mascali D, Mauro GS, Oliva D, Pappalardo AD, Suarez J and Vinciguerra F (2025) Preformed plasma waveguides: Enabling high-energy electron beams for flash radiotherapy. *Nuclear Instruments and Methods in Physics Research Section A* **1081**(170891). doi:10.1016/j.nima.2025.170891
9. Palmer C and Loewen E (2014) *Diffraction Grating Hand-book*, Vol. 7th edn.. Newport Corporation.
10. Henriksen MB, Sigmund F and Johansen TA (2022) A closer look at a spectrographic wavelength calibration 12th Workshop on Hyperspectral Imaging and Signal Processing: Evolution in Remote Sensing (WHISPERS) 13–16 September 2022 IEEE Rome, Italy In *12th Workshop on Hyperspectral Imaging and Signal Processing: Evolution in Remote Sensing (WHISPERS)*, 1–5. doi:10.1109/WHISPERS56178.2022.9955104
11. NIST ASD Team. *Atomic spectra database*. <https://www.nist.gov/pml/atomic-spectra-database>
12. Fujimoto T (2004) *Plasma Spectroscopy*. Oxford University Press.
13. Parigger CG, Drake KA, Helstern CM and Gautam G (2018) Laboratory hydrogen-beta emission spectroscopy for analysis of astrophysical white dwarf spectra. *Atoms* **6**(3), 36. doi:10.3390/atoms6030036
14. Arjmand S, Anania MP, Biagioni A, Costa G, Di Pirro G, Ferrario M, Del Franco M, Galletti M, Del Gorno M, Lollo V, Pellegrini D, Pompili R and Zigler A (2023) Spectral line shape for plasma electron density characterization in capillary tubes. *Journal of Physics: Conference Series* **2439**(1), 012012. doi:10.1088/1742-6596/2439/1/012012
15. Griem HR (1974) *Spectral Line Broadening by Plasmas*. Academic Press, University of Maryland.
16. Gigoso MA and Cardenoso V (1996) New plasma diagnosis tables of hydrogen Stark broadening including ion dynamics. *Journal of Physics B: Atomic, Molecular and Optical Physics* **29**(20), 4795–4838. doi:10.1088/0953-4075/29/20/029
17. Vidal CR, Cooper J and Smith EW (1972) Hydrogen Stark-broadening tables. *Astrophysical Journal Supplement Series* **25**(1973), 37–136. doi:10.1086/190264
18. Touma JE, Oks EA, Alexiou S and Derevianko A (2000) Review of the advanced generalized theory for Stark broadening of hydrogen lines in plasmas with tables. *Journal of Quantitative Spectroscopy and Radiative Transfer* **65**, 543–571/1. doi:10.1016/S0022-4073(99)00095-3
19. Gigoso MA, González MA and Cardenoso V (2003) Computer simulated Balmer-alpha, -beta and -gamma Stark line profiles for non-equilibrium plasmas diagnostics. *Spectrochimica Acta Part B: Atomic Spectroscopy* **58**(8), 1489–1504. doi:10.1016/S0584-8547(03)00097-1
20. Mijatović Z, Djurović S, Gavanski L, Gajo T, Favre A, Morel V and Bultel A (2020) Plasma density determination by using hydrogen Balmer H α spectral line with improved accuracy. *Spectrochimica Acta Part B* **166**, 105821. doi:10.1016/j.sab.2020.105821
21. Wiese WL, Kelleher DE and Paquette DR (1972) Detailed study of the Stark broadening of Balmer lines in a high-density plasma. *Physical Review A* **6**(3), 1132–1153. doi:10.1103/physreva.6.1132
22. Griem HR (2000) Stark broadening of the hydrogen Balmer- α line in low and high density plasmas. *Contributions to Plasma Physics* **40**, 46–56. doi:10.1002/(SICI)1521-3986(200004)40:1/246:AID-CTPP463.0.CO;2-M
23. Jang DG, Kim MS, Nam IH, Uhm HS and Suk H (2011) Density evolution measurement of hydrogen plasma in capillary discharge by spectroscopy and interferometry methods. *Applied Physics Letters* **99**, 141502/14. doi:10.1063/1.3643134
24. Bobrova NA, Esaulov AA, Sakai J-I, Sasorov PV, Spence DJ, Butler A, Hooker SM and Bulanov SV (2001) Simulations of a hydrogen-filled capillary discharge waveguide. *Physical Review E* **65**, 016407. doi:10.1103/PhysRevE.65.016407
25. Arjmand S, Anania MP, Biagioni A, Ferrario M, Franco MD, Galletti M, Lollo V, Pellegrini D, Pompili R and Zigler A (2022) Spectroscopic measurements as diagnostic tool for plasma-filled capillaries. *JACoW IPAC2022*, WEPOST035. doi:10.18429/JACoW-IPAC2022-WEPOST035
26. Gonsalves AJ, Liu F, Bobrova NA, Sasorov PV, Pieronek C, Daniels J, Antipov S, Butler JE, Bulanov SS, Waldron WL, Mittelberger DE and Leemans WP (2016) Demonstration of a high repetition rate capillary discharge waveguide. *Journal of Applied Physics* **119**(3), 033302. doi:10.1063/1.4940121
27. McWhirter RWP (1965) *Plasma Diagnostic Techniques*, Academic Press.
28. Griem HR (1997) *Principles of Plasma Spectroscopy*. Cambridge University Press.
29. Arjmand S, Anania MP, Biagioni A, Ferrario M, Galletti M, Lollo V, Pellegrini D, Pompili R and Zigler A (2023) Different elements, same results: time-resolved temperature determination by oxygen and nitrogen elements. *JINST* **18**(08), P08003. doi:10.1088/1748-0221/18/08/P08003

30. COMSOL multiphysics. <https://www.comsol.com/>
31. Arjmand S, Amato A, Catalano R, Manna C, Mascali D, Mauro GS, Oliva D, Pappalardo AD, Pidatella A, Suarez J, Vinciguerra F and Cirrone GAP (2025) Parametric study of voltage in plasma-discharge capillary systems: a benchmarking of experimental and simulation data. *JINST* **20**(03), C03035. doi:[10.1088/1748-0221/20/03/C03035](https://doi.org/10.1088/1748-0221/20/03/C03035)
32. GEANT4 toolkit. URL: <https://geant4.web.cern.ch>
33. Lee S, Kwon SH, Nam I, Cho MH, Jang D, Suk H and Kim M (2023) One-body capillary plasma source for plasma accelerator research at e-labs. *Applied Sciences* **13**(4), 2564. doi:[10.3390/app13042564](https://doi.org/10.3390/app13042564)
34. Lazzarini CM, Grittani GM, Valenta P, Zymak I, Antipenkov R, Chaulagain U, Goncalves LVN, Grenfell A, Lamač M, Lorenz S, Nevrkla M, Špaček A, Šobr V, Szuba W, Bakule P, Korn G and Bulanov SV (2024) Ultrarelativistic electron beams accelerated by terawatt scalable kHz laser. *Physics of Plasmas* **31**, 030703. doi:[10.1063/5.0189051](https://doi.org/10.1063/5.0189051)